nature communications

Article

https://doi.org/10.1038/s41467-024-53598-3

Interface kinetic manipulation enabling efficient and reliable Mg_3Sb_2 thermoelectrics

Received: 27 June 2024

Accepted: 17 October 2024

Published online: 29 October 2024

Yuntian Fu[1,9], Xin Ai[2,9], Zhongliang Hu[1,9], Shuhan Zhao[3], Xiaofang Lu[1], Jian Huang[4], Aibin Huang[5], Lianjun Wang[1,6], Qihao Zhang[7] & Wan Jiang[1,8]

Development of efficient and reliable thermoelectric generators is vital for the sustainable utilization of energy, yet interfacial losses and failures between the thermoelectric materials and the electrodes pose a significant obstacle. Existing approaches typically rely on thermodynamic equilibrium to obtain effective interfacial barrier layers, which underestimates the critical factors of interfacial reaction and diffusion kinetics. Here, we develop a desirable barrier layer by leveraging the distinct chemical reaction activities and diffusion behaviors during sintering and operation. Titanium foil is identified as a suitable barrier layer for Mg_3Sb_2-based thermoelectric materials due to the creation of a highly reactive ternary MgTiSb metastable phase during sintering, which then transforms to stable binary Ti-Sb alloys during operation. Additionally, titanium foil is advantageous due to its dense structure, affordability, and ease of manufacturing. The interfacial contact resistivity reaches below 5 $\mu\Omega\cdot cm^2$, resulting in a Mg_3Sb_2-based module efficiency of up to 11% at a temperature difference of 440 K, which exceeds that of most state-of-the-art medium-temperature thermoelectric modules. Furthermore, the robust Ti foil/$Mg_3(Sb,Bi)_2$ joints endow Mg_3Sb_2-based single-legs as well as modules with negligible degradation over long-term thermal cycles, thereby paving the way for efficient and sustainable waste heat recovery applications.

Driven by the increasing demand for renewable energy and carbon neutrality, thermoelectric technology, which can convert waste heat directly into electricity based on the Seebeck effect, has attracted increasing attention as a promising solution to improve the utilization efficiency of fossil fuels and reduce the emission of carbon dioxide. Over the past two decades, there has been remarkable progress in the development of thermoelectric materials, leading to the thermoelectric dimensionless figure of merit, known as zT, exceeding 2.0 and even surpassing the unprecedented level of 2.5 in multiple material systems such as SnSe, GeTe, and PbTe[1–3]. These advancements have been an important impetus driving thermoelectric technology into widespread applications. However, in contrast to the rapid development of thermoelectric materials, progress in thermoelectric devices has lagged behind. Most existing thermoelectric devices

[1]State Key Laboratory for Modification of Chemical Fibers and Polymer, Materials & College of Materials Science and Engineering, Donghua University, Shanghai, China. [2]Leibniz Institute for Solid State and Materials Research Dresden e.V. (IFW-Dresden), Dresden, Germany. [3]School of Computer Science, Faculty of Engineering, The University of Sydney, Sydney, NSW, Australia. [4]Materials Genome Institute, Shanghai University, Shanghai, China. [5]State Key Laboratory of High Performance Ceramics and Superfine Microstructure, Shanghai Institute of Ceramics, Chinese Academy of Sciences, Shanghai, China. [6]Engineering Research Center of Advanced Glasses Manufacturing Technology, Ministry of Education, Donghua University, Shanghai, China. [7]Light Technology Institute, Karlsruhe Institute of Technology, Karlsruhe, Germany. [8]Institute of Functional Materials, Donghua University, Shanghai, China. [9]These authors contributed equally: Yuntian Fu, Xin Ai, Zhongliang Hu. e-mail: huangj@shu.edu.cn; wanglj@dhu.edu.cn; qihao.zhang@kit.edu; wanjiang@dhu.edu.cn

exhibit conversion efficiencies below 10% and suffer from poor cycling reliability[3]. This is mainly attributed to the interface between the thermoelectric material and the electrode, where large contact resistances as well as severe elemental diffusion and reactions occur, especially at elevated temperatures. To address this issue, a general solution is to introduce a barrier layer between the electrode and the thermoelectric material. An ideal barrier layer material should not only provide an interface with low contact resistance to minimize losses in thermoelectric conversion but also with high bonding strength and service inertness to withstand thermal attack during operation. Recently, several strategies, such as powder co-sintering experiments[4–7], interfacial reaction and diffusion energy criteria[8,9], and phase diagram calculations[10–12], have been proposed for the efficient screening of suitable barrier layers. Although these efforts have led to significant progress, materials for accessing thermoelectric interfacial barrier layers that are characterized by both high bonding activity and high operation reliability have rarely been developed.

To date, methods such as magnetron sputtering[13], electroplating[14,15], and sintering[16] have been applied to connect interfacial barrier layer materials with thermoelectric materials. Among them, one-step sintering is gaining wide popularity due to its simplicity and versatility[5,17,18]. Typically, barrier layer powders (or foils) and thermoelectric powders are sequentially placed into a graphite die and then densified using hot pressing or spark plasma sintering to obtain a sandwich-structured pellet. Through this process, the densification of thermoelectric materials and the formation of thermoelectric joints are realized concurrently. Therefore, the sintering regimes, including temperature, duration, and pressure, have a crucial role in determining both the resulting properties of thermoelectric materials and the bonding activity and operation reliability of the interface. It is desirable that the interface be diffusively reactive during sintering, such as forming a robust interfacial reactive layer, to establish strong bonding, whereas in service, the interface becomes unreactive and as weakly diffusive as possible (Fig. 1a). This objective goes beyond the thermodynamics of solid-solid interfaces and lies more in the field of interfacial reactions and diffusion kinetics. In this context, temperature is one of the most crucial factors, which is reflected by the one-step sintering temperature (T_s) and the thermoelectric device operating temperature (T_o). Assuming that T_s is greater than T_o, the materials will exhibit higher chemical reaction activity and diffusion kinetics during the sintering process than during the operating process. This implies that the sintering process has the capability to provide enough energy to overcome the reaction and diffusion energy barriers between barrier layers and thermoelectric materials, resulting in the formation of interfacial products. On the other hand, during device service, the diffusion-controlled reaction process can be impeded due to the lower energy provided. By utilizing this kinetic difference, an ideal thermoelectric interface that combines strong bonding and service inertness can be achieved (Fig. 1b).

Based on this envision, we compared the T_s and T_o of a variety of thermoelectric materials[1,5,6,8,9,18–50]. It is evident that T_s is much higher than T_o in some thermoelectric systems, as exemplified by Mg_3Sb_2, whose T_s can be 500 K greater than T_o (Fig. 1c). This implies that these materials have distinct chemical reactivity and diffusion rates during sintering and operation. Taking advantage of this kinetic difference, we found that titanium (Ti) foil is a suitable barrier layer for Mg_3Sb_2-based thermoelectric materials owing to its high sintering activity and excellent service inertness, as well as its dense structure, low cost and ease of fabrication. Our study shows that Ti foil reacts with Mg_3Sb_2 to produce a MgTiSb metastable phase at a T_s of 1023 K, whereas no reaction occurs between them when sintered at 748 K (the T_o of

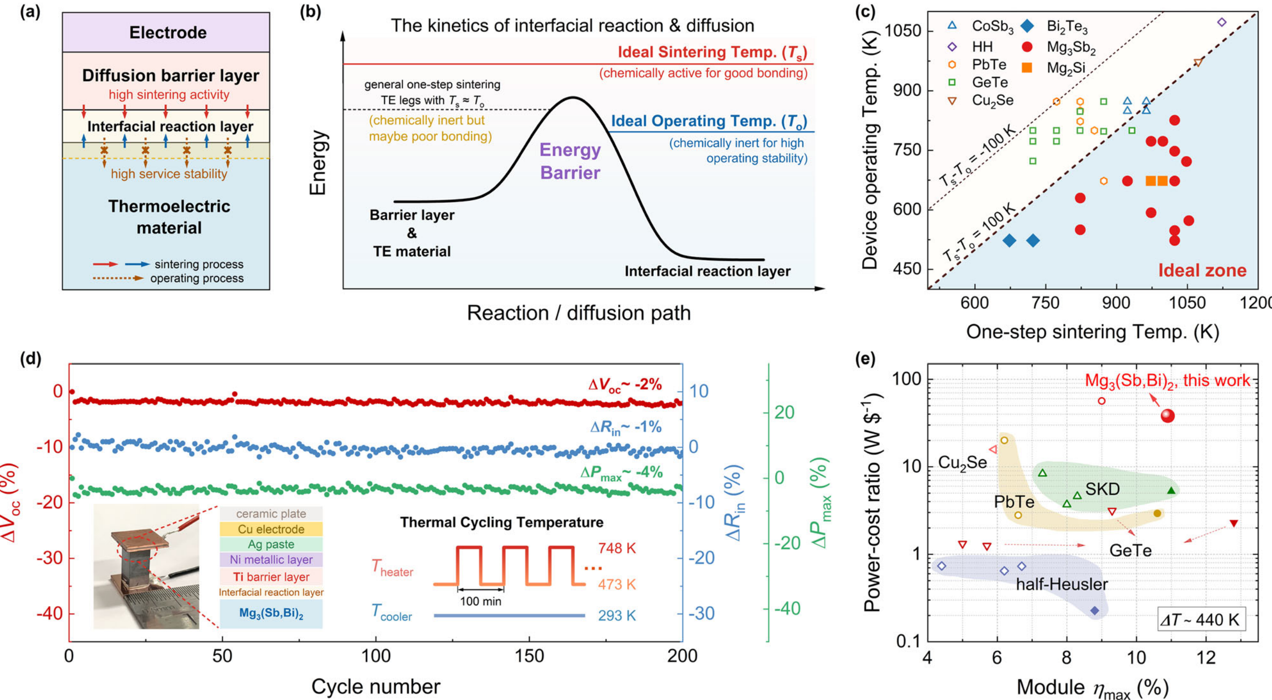

Fig. 1 | Design of the thermoelectric barrier layer and the resulting robust Mg_3Sb_2-based devices. a Schematic diagram of the most desirable thermoelectric barrier layer featuring high sintering activity and high service reliability. **b** Design of the thermoelectric barrier layer by utilizing kinetic differences during sintering and operation. TE is an abbreviation for thermoelectric. **c** One-step sintering temperature (T_s) and thermoelectric device operating temperature (T_o) of various thermoelectric materials[1,5,6,8,9,18–50]. HH is an abbreviation for half-Heusler. **d** Changes in the open-circuit voltage (V_{oc}), device resistance (R_{in}), and maximum output power (P_{max}) of a Mg_3Sb_2-based single leg during thermal cycling testing. The inset shows a photograph of the single leg, and illustrates the cycling temperature regime, where the heat-source temperature (T_{heater}) cycles between 473 K and 748 K while the cold-side temperature (T_{cooler}) is maintained at 293 K. **e** Comparisons of the cost-effectiveness and maximum conversion efficiency (η_{max}) of different thermoelectric modules at a temperature difference (ΔT) of ~440 K[5,9,19,22,51,52].

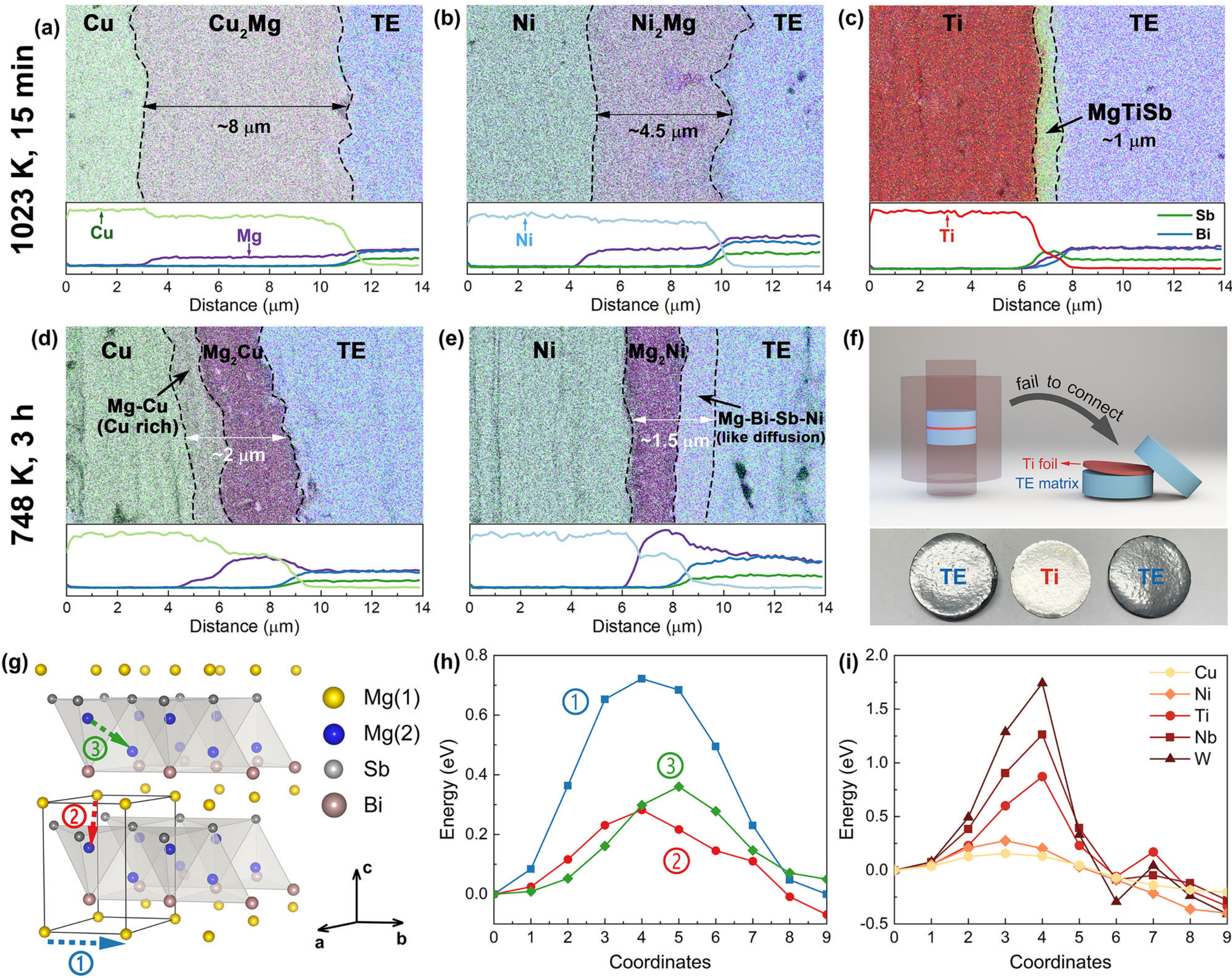

Fig. 2 | Interfacial diffusion and reaction at different one-step sintering temperatures. EDS mapping and line scanning results showing the elemental distribution of (**a**) Cu, (**b**) Ni, and (**c**) Ti foil sintered with $Mg_3(Sb,Bi)_2$ at 1023 K for 15 min. TE stands for $Mg_3(Sb,Bi)_2$. EDS mapping and line scanning results of (**d**) Cu and (**e**) Ni sintered with $Mg_3(Sb,Bi)_2$ at 748 K for 3 h. **f** Schematic and photograph of Ti foil sintered with $Mg_3(Sb,Bi)_2$ at 748 K for 3 h, showing the inertness of Ti foil with $Mg_3(Sb,Bi)_2$-based materials at 748 K. **g** Migration channels of Mg atoms in $Mg_3(Sb,Bi)_2$ and (**h**) corresponding energy barrier along these channels. **i** Energy barrier for the migration of several metals within the $Mg_3(Sb,Bi)_2$ lattice.

Mg_3Sb_2). The MgTiSb phase leads to an initial interfacial contact resistivity of less than 5 μΩ·cm^2, which is among the lowest ever reported. During accelerated thermal ageing tests, MgTiSb transforms into different Ti-Sb phases at different ageing temperatures, whereas the thickness of the interfacial reactive layer remains almost constant, and the contact resistivity remains low. A Mg_3Sb_2-based single-leg thermoelectric device was subsequently fabricated for reliability evaluation. Its power generation performance keeps stable throughout 200 thermal cycles lasting 330 h with heat-source temperature (T_{heater}) cycling between 473 K and 748 K (Fig. 1d), demonstrating excellent reliability. Furthermore, a module efficiency of up to 11% is achieved at T_{heater} of 723 K and a temperature difference (ΔT) of 440 K in a Mg_3Sb_2-based thermoelectric module, which surpasses that of most state-of-the-art medium-temperature thermoelectric modules[5,9,19,22,51,52] (Fig. 1e). Moreover, our module contains no toxic elements and has a superior power/cost ratio compared to existing modules (Fig. 1e), indicating significant promise for widespread applications.

Results

Interface kinetic differences during sintering and operation

The results of powder co-sintering experiments reported in our previous work show that Cu, Ni, and Ti can form interfacial reaction layers with $Mg_3(Sb,Bi)_2$ during the densification process of $Mg_3(Sb,Bi)_2$[5]. This implies that these three elements have high sintering activity as the diffusion barrier layer. To determine whether they possess excellent stability during operation, we sintered Cu, Ni, and Ti foils with $Mg_3(Sb,Bi)_2$ in one step at 1023 K (the T_s of $Mg_3(Sb,Bi)_2$) and 748 K (the T_o of $Mg_3(Sb,Bi)_2$), and studied their interfacial reactions and diffusion behaviors in detail.

As a result, at 1023 K with a holding time of 15 min, the Cu, Ni and Ti foils react with $Mg_3(Sb,Bi)_2$ (Fig. 2a–c). The interfacial reaction products are Cu_2Mg, Ni_2Mg, and MgTiSb compounds, respectively (Supplementary Table 1). This suggests that Mg is highly active in the reaction of $Mg_3(Sb,Bi)_2$ with metal foils and that the formation of Mg-based compounds are preferred. The thicknesses of the interfacial reaction layer for Cu, Ni, and Ti are 8 μm, 4.5 μm, and 1 μm, respectively, indicating that the reaction rates follow the order of Cu > Ni > Ti.

In contrast, when the samples were sintered at 748 K (the typical maximum operating temperature of $Mg_3(Sb,Bi)_2$) for up to 3 h, Cu and Ni still react with $Mg_3(Sb,Bi)_2$ (Fig. 2d, e); however, the Ti foil is unable to connect with $Mg_3(Sb,Bi)_2$ (Fig. 2f). The interfacial reaction layer in the case of Cu foil consists of a Mg-Cu diffusion layer and a Mg_2Cu reaction layer, whereas in the case of Ni foil, it consists of a Mg_2Ni reaction layer and a Mg-Sb-Bi-Ni diffusion layer (Supplementary

Table 2). The interfacial products formed at 748 K exhibit distinct composition and thickness compared to those formed at 1023 K, clearly demonstrating the pronounced temperature dependence of the interfacial reaction and diffusion kinetics. The failure of Ti foil to connect with $Mg_3(Sb,Bi)_2$ even after prolonged sintering time suggests that Ti foil is inert to $Mg_3(Sb,Bi)_2$ at a service temperature of 748 K. Therefore, it can act as a diffusion barrier to achieve high interfacial stability.

We also sintered the Ti foil with $Mg_3(Sb,Bi)_2$ at 923 K to explore the activation temperature of the reaction between them. The findings indicate that a reaction layer with a thickness of only 500 nm is formed at the interface after holding at 923 K for 30 min (Supplementary Fig. 1a). The composition of the reaction layer is also MgTiSb (Supplementary Fig. 1b, c), which is identical to the composition achieved during sintering at 1023 K. This result suggests that the reaction between Ti and $Mg_3(Sb,Bi)_2$ preferentially produces the ternary MgTiSb compound, and the activation temperature should be slightly below 923 K but significantly above 748 K. Hence, the Ti foil is characterized by both high sintering activity and service inertness for $Mg_3(Sb,Bi)_2$.

Density functional theory (DFT) calculations were further performed to elucidate the interface kinetic differences. First, the vacancy formation energies of a number of barrier layer candidates (Cu, Ni, Ti, Fe, Nb, Cr, Mo, and W) as well as different sites of $Mg_3(Sb,Bi)_2$ were calculated. As shown in Supplementary Table 3, the vacancy formation energy at the Mg1 site of $Mg_3(Sb,Bi)_2$ is the lowest. Thus, the vacancy flux tends to shift from the pure metals toward the $Mg_3(Sb,Bi)_2$ side, as reflected by the Kirkendall effect[53]. The energy barriers for atomic diffusion within $Mg_3(Sb,Bi)_2$ were then determined by the climbing image nudged elastic band (CI-NEB) method[54]. Three different diffusion paths for Mg-Mg migration were compared (Fig. 2g). Among them, path ② from the Mg1 to Mg2 sites exhibits the lowest migration barrier (Fig. 2h). Therefore, we selected this path to further investigate the diffusion behavior of different metals within $Mg_3(Sb,Bi)_2$. As shown in Fig. 2i, among the five selected metals, W and Nb exhibit significantly higher energy barriers with double peaks when moving from one vacancy to neighboring sites in $Mg_3(Sb,Bi)_2$. In contrast, Ni and Cu diffuse more easily within the $Mg_3(Sb,Bi)_2$ lattice, while Ti displays a moderate migration barrier. This suggests that it is challenging for $Mg_3(Sb,Bi)_2$ to form interfacial compounds with W and Nb, whereas Ni and Cu can induce rapid interfacial growth. The case of Ti lies in between, resulting in a moderate growth of the interface. These calculated results are consistent with our experimental results of previous powder co-sintering[5] and the one-step sintering here. In addition, all these diffusion barrier values are lower than the self-diffusion energy barriers in pure metals (Supplementary Table 3), suggesting that diffusion occurs via one-way migration from the metal side to the $Mg_3(Sb,Bi)_2$ side.

Interfacial evolution of Ti/$Mg_3(Sb,Bi)_2$ joints

According to our previous work, $Mg_3(Sb,Bi)_2$ can work stably at 748 K[5]. Above this temperature, the Mg element volatilizes severely, leading to deterioration of the thermoelectric properties[55,56]. Therefore, to evaluate the interfacial service stability of Ti/$Mg_3(Sb,Bi)_2$, we performed thermal ageing tests on the joints at 748 K. To obtain the interfacial evolution behavior in a shorter period of time, we also performed accelerated thermal ageing experiments, i.e., thermal ageing of the joints at temperatures of 773 K, 798 K, and 823 K, which are much higher than their service temperature.

As a result, even after accelerated thermal ageing at 798 K for 360 h, the Ti foil is still well connected to the $Mg_3(Sb,Bi)_2$ matrix, and no cracks are formed between them (Fig. 3a). More crucially, no further diffusion of elements was observed, and the thickness of the interfacial reaction layer hardly increases (Supplementary Fig. 2), indicating the good service stability of the interface. Note that this is quite different from the result of using Ti powder as a barrier layer. Initially, the contact resistivity of the $Mg_3(Sb,Bi)_2$/Ti powder interface is 6.5 $\mu\Omega \cdot cm^2$, which is comparable to that of the $Mg_3(Sb,Bi)_2$/Ti foil interface (Supplementary Fig. 3). These values indicate that both Ti powder and Ti foil provide similarly low initial contact resistivity after being sintered with $Mg_3(Sb,Bi)_2$. However, significant differences arise after thermal ageing at 798 K for 360 h. The Ti powder/$Mg_3(Sb,Bi)_2$ interface shows the formation of complete cracks (Fig. 3b), resulting in electrical disconnection. Compared to the Ti foil, the Ti powder shows a poor service stability. We notice that Ti powder is not sintered into a dense layer after sintering at 1023 K, and $Mg_3(Sb,Bi)_2$ is present inside the Ti layer (Supplementary Fig. 4). Although a reaction layer with the same composition as that used for Ti foil is formed at each interface between the Ti powder and $Mg_3(Sb,Bi)_2$, its thickness increases to 2–5 μm. This indicates that more intense reactions and diffusion occur at the interfaces between the Ti powder and $Mg_3(Sb,Bi)_2$ than that of Ti foil, which is related to the increased rate caused by the increased diffusion channels and reaction interfaces. However, unlike in the case of loose Ti powder, there is only one interface between the dense Ti foil and $Mg_3(Sb,Bi)_2$, which greatly mitigates the interfacial reactions and diffusion during service.

Moreover, we find that the composition of the interfacial reaction layer changes with increasing thermal ageing temperature (Fig. 3c). The interfacial reaction product after sintering is ternary MgTiSb, as confirmed by XRD, TEM images, selected area electron diffraction patterns, and elemental analysis (Fig. 3d–g, Supplementary Figs. 5, 6 and Table 4). TEM characterization also reveals some Mg enrichment between the Ti foil and Ti-Sb diffusion layer. Upon ageing at 748 K, the MgTiSb compound near the Ti foil partially changes to Ti_2Sb, while the interfacial reaction layer mostly changes to Ti_2Sb when the ageing temperature is increased to 773 K and 798 K (Fig. 3h, Supplementary Fig. 7). According to the ternary phase diagram of Mg-Ti-Sb in the Open Quantum Materials Database (OQMD) database (Supplementary Fig. 8), MgTiSb can be decomposed into Mg, Ti_2Sb and Mg_3Sb_2. Therefore, we suppose that the compositional changes during thermal ageing are due to the volatilization of Mg. This is also in agreement with the calculated formation energy results that Ti_2Sb has a more negative value than MgTiSb (Supplementary Table 5), i.e., Ti_2Sb is more stable. In addition, the thickness of the interfacial reaction layer does not increase significantly during thermal ageing up to 798 K (Supplementary Fig. 9), suggesting that the interface maintains high stability below 798 K. As the ageing temperature further increases to 823 K, the interfacial reaction layers change to Ti_5Sb_2 and Ti_5Sb_3 (Fig. 3i), while the thickness increases abnormally and there is a risk of failure. The detailed interfacial evolution at 823 K requires further study. However, considering that the usual operating temperature of $Mg_3(Sb,Bi)_2$ is ~748 K, Ti foil is sufficient for the application of $Mg_3(Sb,Bi)_2$ for mid-temperature thermoelectric power generation. Note that we attempted to synthesize MgTiSb for more characterizations, but have not succeeded in obtaining the pure phase (Supplementary Fig. 10). Similar difficulties have been reported for other ternary compounds, such as MgNiSb[11], highlighting the challenges associated with synthesizing these ternary compounds. Furthermore, from a practical standpoint, forming MgTiSb in situ by directly using Ti foil and $Mg_3(Sb,Bi)_2$ through a one-step sintering process is more convenient and cost-effective. This method avoids the complexities and additional steps involved in synthesizing and handling complex multicomponent compounds.

Given the significant reaction between Ti and $Mg_3(Sb,Bi)_2$, the reaction equation should be better understood. For this purpose, we used tungsten powder, which is chemically inert to $Mg_3(Sb,Bi)_2$, as a marker for the initial position of the Ti/$Mg_3(Sb,Bi)_2$ interface. Tungsten powder was pre-sintered with $Mg_3(Sb,Bi)_2$ to prevent it from being pressed into Ti foil during sintering. With the help of the tungsten marker, we observe that the interfacial reaction layer is located inside

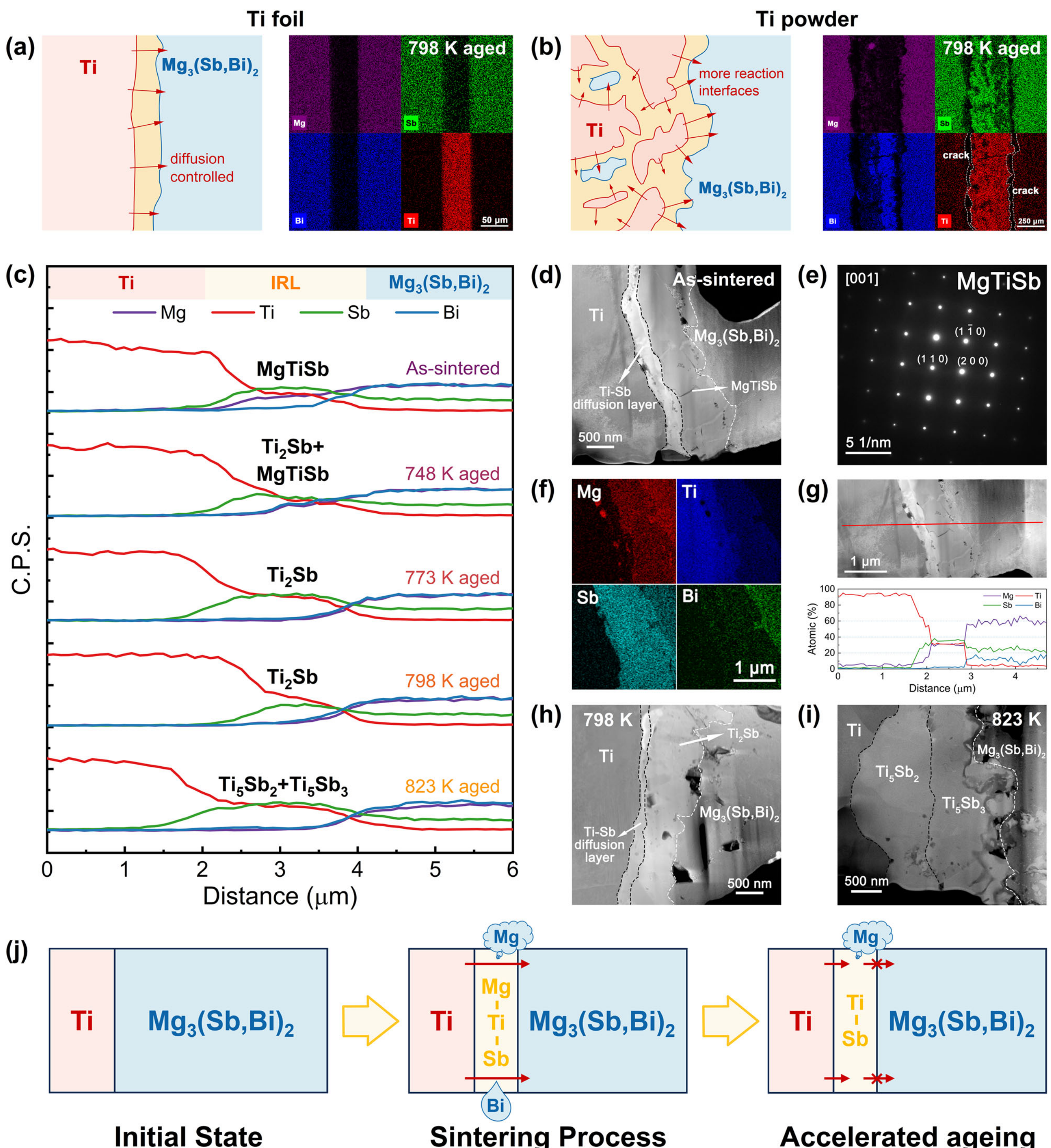

Fig. 3 | Interfacial stability of Ti foil/$Mg_3(Sb,Bi)_2$ joints. a Ti foil/$Mg_3(Sb,Bi)_2$ joint after thermal ageing at 798 K for 360 h. **b** Ti powder/$Mg_3(Sb,Bi)_2$ joint after thermal ageing at 798 K for 360 h. **c** EDS line scanning results showing that the interfacial reaction layer (IRL) changes when ageing at different temperatures for 360 h. Microstructural characterization of the as-sintered Ti foil/$Mg_3(Sb,Bi)_2$ joint: **d** TEM image; **e** Selected area electron diffraction (SAED) pattern; **f** Elemental mapping; **g** Elemental line scanning. **h** TEM image of the Ti foil/$Mg_3(Sb,Bi)_2$ joint after thermal ageing at 798 K for 360 h. **i** TEM result of Ti foil/$Mg_3(Sb,Bi)_2$ after thermal ageing at 823 K for 360 h. **j** Schematic diagram of the Ti foil/$Mg_3(Sb,Bi)_2$ interfacial reaction and diffusion during sintering and thermal ageing.

the $Mg_3(Sb,Bi)_2$ matrix (Supplementary Fig. 11), suggesting that the formation of the MgTiSb product results from the diffusion of Ti into $Mg_3(Sb,Bi)_2$. This is consistent with the DFT calculations above. Considering the conservation of matter, it can be deduced that the formation of MgTiSb is accompanied by the precipitation of Bi and precipitation/volatilization of Mg. Therefore, we can write the reaction equation as: $Mg_3SbBi + Ti = MgTiSb + Bi + 2Mg$. This also explains the presence of pores and Bi enrichment after thermal ageing when using Ti powder as a diffusion barrier (Supplementary Fig. 4). A corresponding schematic diagram of the interfacial evolution is shown in Fig. 3j.

Interfacial electrical properties

In light of the robust connection between the Ti foil and the $Mg_3(Sb,Bi)_2$ matrix and the excellent interfacial stability, we expect that the contact resistivity before and after thermal ageing will also be

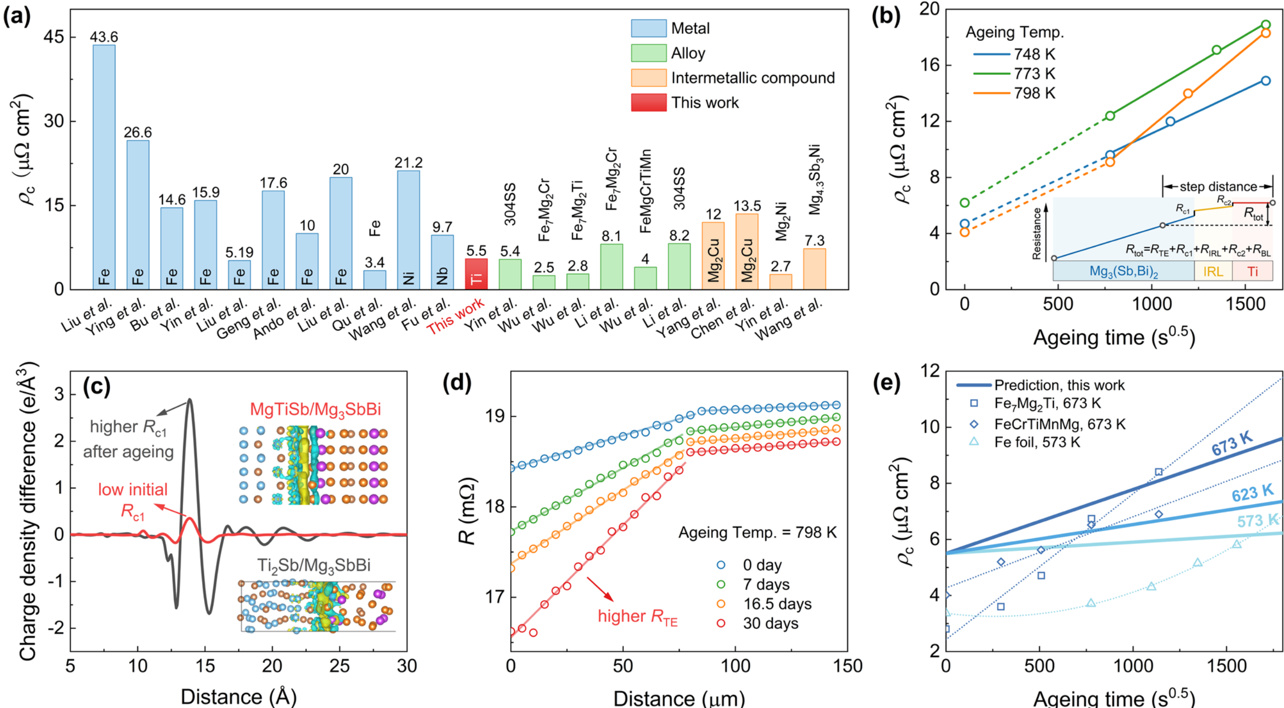

Fig. 4 | Interfacial electrical properties. a Contact resistivity of the as-sintered Ti foil/$Mg_3(Sb,Bi)_2$ joint in comparison with literature results[5,10,12,19–26,51,55,66–70]. **b** Contact resistivity of the Ti foil/$Mg_3(Sb,Bi)_2$ joint under different thermal ageing temperature and time. The inset shows that the measured resistances near the interface (R_{tot}) include the resistances of $Mg_3(Sb,Bi)_2$ (R_{TE}), the interfacial reaction layer (R_{IRL}), the Ti foil barrier layer (R_{BL}), and the contact resistance (R_c). **c** Planar charge density difference as a function of the z-axis distance of MgTiSb/$Mg_3(Sb,Bi)_2$ and Ti_2Sb/$Mg_3(Sb,Bi)_2$ interfaces. The inset shows the charge density differences perpendicular to the MgTiSb and Ti_2Sb interfaces after full atomic relaxation. The (001) plane of $Mg_3(Sb,Bi)_2$ was selected to interface with the low-index planes of MgTiSb and Ti_2Sb. **d** Linear scanning of resistance across the junctions for estimating the contact resistivity, where the slope reflects the material's intrinsic resistivity. **e** Predicted contact resistivity of the Ti foil/$Mg_3(Sb,Bi)_2$ joint at different operating temperatures over time. Experimental data from the literature are included for comparison[55,66,68].

very favorable. As expected, the as-sintered Ti foil/$Mg_3(Sb,Bi)_2$ joint possesses an average contact resistivity as low as 5.5 μΩ·cm² (Fig. 4a), which is lower than our previously reported contact resistivity when using Nb foil (9.7 μΩ·cm²)[5]. Compared to all existing diffusion barrier materials for $Mg_3(Sb,Bi)_2$, including metals, alloys, and intermetallic compounds, our Ti foil/$Mg_3(Sb,Bi)_2$ joint is among the best. Although some alloys present lower contact resistivity, their compositional complexity and difficulty in one-step sintering limit their practical application.

After accelerated thermal ageing, the contact resistivity of the Ti foil/$Mg_3(Sb,Bi)_2$ joint increases but remains as low as 14.9, 18.9, and 18.3 μΩ·cm² after ageing at 748 K, 773 K, and 798 K for 720 h, respectively (Fig. 4b). These values are even lower than the initial contact resistivities when some metals, such as Fe and Ni, are used as barrier layers (Fig. 4a). The current-voltage characteristics of the Ti foil/$Mg_3(Sb,Bi)_2$ joints, both before and after ageing, exhibit a linear relationship (Supplementary Fig. 12), indicating that all interfaces form ohmic contacts. More notably, the contact resistivity is linearly related to the square root of the ageing time (Fig. 4b), from which we can infer that the evolution of the Ti/$Mg_3(Sb,Bi)_2$ interface is a diffusion-controlled process[57]. However, the increase in the contact resistivity contradicts the TEM results above, which show little change in the thickness of the interfacial reaction layer after thermal ageing. We attribute this to the fact that the scanning step (5 μm) during the contact resistivity measurement is larger than the thickness (less than 3 μm, Fig. 3a) of the interfacial reaction layer. In this case, the resistance measured near the interface (R_{tot}) is composed of the resistance of the $Mg_3(Sb,Bi)_2$ thermoelectric material (R_{TE}), interfacial reaction layer material (R_{IRL}), and Ti foil barrier layer (R_{BL}), as well as the contact resistance of the $Mg_3(Sb,Bi)_2$/IRL interface (R_{c1}) and IRL/Ti foil (R_{c2}) interface, i.e., $R_{tot} = R_{TE} + R_{c1} + R_{IRL} + R_{c2} + R_{BL}$ (the inset of Fig. 4b). The measured contact resistivity is calculated by $\rho_c = R_{tot} \times A$, where A is the cross-sectional area of the sample. Therefore, an increase in the resistance of any portion will lead to an increase in the final measured contact resistivity. Due to the metallic nature of the MgTiSb and Ti_2Sb interfacial reaction layers (Supplementary Figs. 13 and 14) as well as the Ti barrier layer, the resistances of the R_{IRL}, R_{c2}, and R_{BL} are relatively low and can be neglected. The increase in the measured contact resistivity thus mainly originates from the increase in the R_{TE} and R_{c1}.

In order to clarify the R_{c1} of the MgTiSb/$Mg_3(Sb,Bi)_2$ and Ti_2Sb/$Mg_3(Sb,Bi)_2$ interfaces, we calculated their potential interfacial configurations and the associated electron transport. As shown in Fig. 4c, the peak value of the charge density difference at the MgTiSb/$Mg_3(Sb,Bi)_2$ interface is significantly lower than that at the Ti_2Sb/$Mg_3(Sb,Bi)_2$ interface, implying that the interfacial contact resistance of the former is lower. This means that MgTiSb can effectively reduce the fluctuation of charge density for electrons transferring through the interface from the metal side to the $Mg_3(Sb,Bi)_2$ side, thereby weakening electron scattering. This explains the low contact resistivity of the as-sintered Ti foil/$Mg_3(Sb,Bi)_2$ joint. In contrast, the larger charge density difference at the Ti_2Sb/$Mg_3(Sb,Bi)_2$ interface results in an increase in R_{c1} after accelerated thermal ageing, which increases the measured contact resistivity. To further support this, we studied the distribution profile of the macroscopic average potential at the interfaces between $Mg_3(Sb,Bi)_2$ and MgTiSb, Ti_2Sb, or Ti_5Sb_3, which is believed to correlate strongly with contact resistance[58]. As shown in Supplementary Fig. 15, the analyzed potential transitions more gradually from the formation interlayer to the $Mg_3(Sb,Bi)_2$ side, exhibiting a smaller relevant value at the $Mg_3(Sb,Bi)_2$/MgTiSb interface compared to the Ti_2Sb and Ti_5Sb_3 interfaces. This observation aligns with the

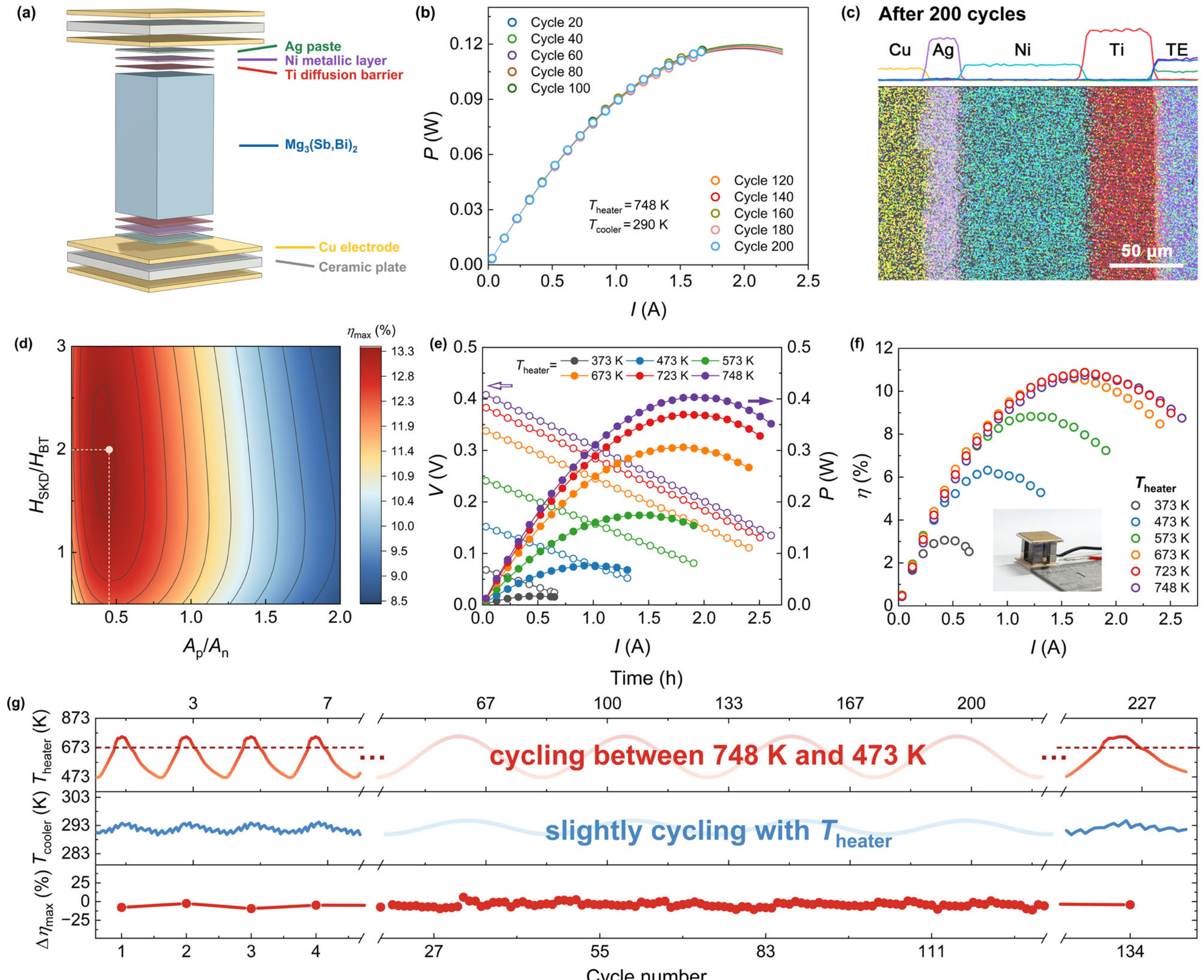

Fig. 5 | Power generation performance and reliability of the $Mg_3(Sb,Bi)_2$-based single-leg and module. **a** Schematic diagram of a thermoelectric single-leg using $Mg_3(Sb,Bi)_2$. **b** Output power as a function of current for $Mg_3(Sb,Bi)_2$ single-leg after different thermal cycles. **c** EDS mapping result of the hot-side interface of the $Mg_3(Sb,Bi)_2$ single-leg after 200 thermal cycles. **d** Structural design of a thermoelectric module consisiting of n-type $Mg_3(Sb,Bi)_2$ and p-type $CoSb_3$-Bi_2Te_3 segmented legs for maximum conversion efficiency at T_{heater} = 748 K and T_{cooler} = 283 K. Voltage, power (**e**) and conversion efficiency (**f**) as a function of current under different heat source temperatures. The inset of (**f**) shows a photograph of a $Mg_3(Sb,Bi)_2$/$CoSb_3$-Bi_2Te_3 module. **g** Thermal cycling test of the $Mg_3(Sb,Bi)_2$/$CoSb_3$-Bi_2Te_3 module.

trend identified for the charge density difference. In addition, due to the high saturation vapor pressure of Mg element, the $Mg_3(Sb,Bi)_2$ matrix inevitably deteriorates at such high temperatures (≥748 K) and under vacuum (<1 Pa) over time, leading to an increase in R_{TE}, as reflected by the gradually increasing slope in Fig. 4d. Based on these results, we can claim that (i) the actual interfacial contact resistivity using titanium foil as a barrier layer should be lower than our current measurements, i.e., the initial contact resistivity must be below 5 μΩ·cm^2, and (ii) the rate of increase in the single interfacial contact resistivity with ageing time is much slower.

The four-probe scanning resistance measurements include the changes in the interfacial contact resistivity and thermoelectric material resistivity, from which we derived the activation energy for contact resistivity growth which more closely corresponds to the actual service conditions (Supplementary Fig. 16). In addition, since thermal ageing of $Mg_3(Sb,Bi)_2$-based joints at such high temperatures (≥748 K) has rarely been reported, we further predicted the contact resistivity of Ti foil/$Mg_3(Sb,Bi)_2$ joints at lower temperatures (e.g., 573 K, 623 K, and 673 K) over time for comparison with existing reports. Encouragingly, although the initial contact resistivity of the Ti foil/$Mg_3(Sb,Bi)_2$ joint is slightly higher than that of multielement alloy barrier layers, its rate of increase is significantly lower (Fig. 4e). The retarded increase in the contact resistivity is essential for the preparation of long-life and highly stable thermoelectric devices. In this regard, the Ti foil diffusion barrier layer stands out for its excellent service stability with $Mg_3(Sb,Bi)_2$ owing to the low reaction and diffusion rates, as well as its lower cost and easier fabrication compared to other candidate materials.

Device fabrication and performance evaluation

To further evaluate the feasibility of using Ti foil as a barrier layer for $Mg_3(Sb,Bi)_2$, we fabricated a $Mg_3(Sb,Bi)_2$-based thermoelectric single leg (Fig. 5a), in which nickel was used as a metallic connecting layer to improve the soldering activity of Ti/$Mg_3(Sb,Bi)_2$ joint with the silver paste. Thermal cycling experiments were performed to examine the long-term reliability. During the measurements, the cold-side temperature (T_{cooler}) was maintained at 293 K, while the heat-source temperature (T_{heater}) was cycled between 473 K and 748 K (Fig. 1d). One cycle lasted 100 min, and the device power generation performance was measured whenever T_{heater} was stabilized at 748 K. Measurements

were carried out in a chamber under vacuum. As a result, there was no deterioration in the output voltage or internal resistance after 200 cycles (~330 h, Fig. 1d and Supplementary Fig. 17). The output power-current curve is comparable to that before thermal cycling (Fig. 5b). The $Mg_3(Sb,Bi)_2$ single leg exhibits excellent service stability/durability during long-term thermal cycling. It is worth noting that, in contrast to the accelerated thermal ageing of Ti/$Mg_3(Sb,Bi)_2$ joints at constant temperatures, thermal cycling tests additionally involve the evaluation of material thermal fatigue and the ability of the interface to withstand thermal stresses. Despite the mismatch in the coefficient of thermal expansion (CTE) between Ti foil and $Mg_3(Sb,Bi)_2$ (Supplementary Fig. 18), our thermal cycling measurements do not show significant performance degradation or interface cracking, suggesting that the interface bond strength is sufficient to withstand thermal stress. This is partly attributed to the thin thickness of the barrier layer, where a Ti foil is 30 μm and an interfacial reaction layer is only 2 μm, effectively mitigating the thermal stress resulting from the CTE mismatch. On the other hand, recent studies highlight the high fracture toughness and plastic properties of $Mg_3(Sb,Bi)_2$[59–61], which also contributes to its tolerance for CTE mismatch. This is further confirmed by characterizing the hot-side interfaces of the $Mg_3(Sb,Bi)_2$ leg after 200 thermal cycles. The SEM results (Supplementary Fig. 19) show that all the interfaces are well connected, with no fractures or holes generated. Elemental mapping and line scanning reveal that no significant elemental diffusion or reaction occurred at the interfaces during thermal cycling (Fig. 5c). The atomic ratio of $Mg_3(Sb,Bi)_2$ after thermal cycling measurements is consistent with the composition before thermal cycling (Supplementary Fig. 20). The interfacial reaction layer between Ti and $Mg_3(Sb,Bi)_2$ still contains MgTiSb, which is consistent with the above result of the interfacial thermal ageing test at 748 K.

It should be noted that we do not show the efficiency of the thermoelectric single leg because we recognize that the single-leg efficiency can be inaccurately measured due to large errors in heat flow. In addition, since a single leg cannot be used solely, its efficiency holds less practical significance. Therefore, we proceeded to construct thermoelectric modules by combining n-type $Mg_3(Sb,Bi)_2$-based legs with p-type $CoSb_3$-Bi_2Te_3 segmented legs in order to showcase their application potential. Prior to fabrication, finite element simulations were conducted to determine the geometrical configuration of the thermoelectric module, particularly the height ratio of p-type $CoSb_3$ to p-type Bi_2Te_3 (H_{SKD}/H_{BT}) and the cross-sectional area ratio of the p- and n-type legs (A_p/A_n). As a result, the simulated maximum conversion efficiency (η_{max}) reaches 13% at $H_{SKD}/H_{BT} = 2$ and $A_p/A_n = 0.45$ at $T_{heater} = 748$ K and $T_{cooler} = 283$ K (Fig. 5d and Supplementary Fig. 21). Based on the optimization, we fabricated a two-pair module with module dimensions of 10 mm × 10 mm. The n-type leg is 3 × 3 × 6 mm^3 and the p-type leg is 2 × 2 × 6 mm^3. The measured output voltage (V) exhibits a good linear relationship with the current (I) (Fig. 5e), where the y-intercept and slope of the V-I plot correspond to the open-circuit voltage (V_{oc}) and the module's internal resistance (R_{in}), respectively. The output power curve reaches its peak when the resistance of the external load is equivalent to R_{in}. Experimentally, a maximum output power (P_{max}) of 0.4 W is obtained at $I = 2$ A and $\Delta T = 465$ K, while an efficiency reaching 11% is achieved when $T_{heater} = 723$ K and $\Delta T = 440$ K (Fig. 5f). The peak efficiency slightly decreases to 10.5% when T_{heater} rises to 748 K due to the overestimation of heat flow (Q_c) caused by heat radiation.

Thermal cycling experiments were also conducted on the module to evaluate its long-term reliability. Throughout the cycling period, T_{cooler} was maintained at 293 K, while T_{heater} cycled between 473 K and 748 K. After 135 cycles (~225 h), P_{max} and η_{max} show negligible drop of ~2% and 4%, respectively (Fig. 5g and Supplementary Fig. 22). Notably, although efficiency measurements at temperatures as high as 748 K have been made on $Mg_3(Sb,Bi)_2$-based modules, achieving exceptional thermal cycling stability at such high temperatures has never been reported before.

Discussion

In conclusion, the advancement of thermoelectric devices for widespread commercial application has been hindered by the quest for effective and reliable interfacial barrier materials. In this work, we overcome the constraints imposed by thermodynamic equilibrium to identify desirable thermoelectric barrier layer materials through a kinetic transition from a high-temperature metastable phase to a low-temperature stable phase. By exploiting the contrasting kinetic properties of the reaction and diffusion behaviors between $Mg_3(Sb,Bi)_2$ and Ti during sintering and operation, we achieve exceptional sintering activity and excellent service inertness in Ti foil/$Mg_3(Sb,Bi)_2$ joints. The interfacial contact resistivity is reduced to below 5 μΩ·cm^2, leading to a module efficiency of 11% at T_{heater} of 723 K. Furthermore, the single-leg and modules based on Mg_3Sb_2 exhibit exceptional long-term durability when subjected to thermal cycling. Our work provides a pathway to address the long-standing bottleneck of developing efficient and stable interface materials for durable energy conversion and storage.

Methods

Material preparation

The n-type $Mg_3(Sb,Bi)_2$ and p-type $Ce_{0.9}Fe_3CoSb_{12}$ were synthesized following our previous work[5,62]. Different diffusion barrier layer materials were investigated in samples with a sandwiched structure of $Mg_3(Sb,Bi)_2$/M/$Mg_3(Sb,Bi)_2$ (where M represents Cu, Ni, and Ti). Herein, Cu foil (Hebei Zhanmo Metal Materials Ltd., 99.9%, 50 μm), Ni foil (Hebei Zhanmo Metal Materials Ltd., 99.9%, 50 μm), Ti powder (99.99%, Macklin, 300 mesh), and Ti foil (Hebei Zhanmo Metal Materials Ltd., 99.9%, 50 μm) were compacted with $Mg_3(Sb,Bi)_2$ powders, respectively, by hot-press sintering (ZT-40-21Y, Shanghai Chenhua Science Technology Co., Ltd.). Two different sintering regimes were employed: (1) sintering at a temperature of 1023 K for a duration of 15 min, and (2) sintering at a temperature of 748 K for a duration of 3 h. Both had a pressure of 50 MPa. For the thermal ageing studies, samples with a sandwiched structure were sealed in quartz tubes under vacuum and then placed in furnaces (YFX12/10Q-GC, Shanghai Y-Feng Electrical Furnace Co., Ltd.) at different temperatures. There are at least three parallel samples for each test condition.

Fabrication of the $Mg_3(Sb,Bi)_2$ module and single leg

The n-type Ni/Ti/$Mg_3(Sb,Bi)_2$/Ti/Ni and p-type Ni/TiAl/$CoSb_3$ joints were fabricated by one-step sintering under the same conditions as the sintering of the corresponding thermoelectric materials, i.e., the n-type was sintered at 1023 K, a pressure of 50 MPa, and a holding time of 15 min, while the p-type was sintered at 923 K, a pressure of 60 MPa, and a holding time of 1.5 h. Ni foil with a thickness of 100 μm was used as the metallization layer for better soldering with a double-sided direct bonded copper (DBC) alumina plate. The Ti foil and TiAl powder work as diffusion barrier layers. The sintered joints were then cut into dices with dimensions of 3 × 3 × 6 mm^3 for the n-type and 2 × 2 × 4 mm^3 for the p-type. Subsequently, commercial p-type Bi_2Te_3 dices in the dimension of 2 × 2 × 2 mm^3 (with electroplated nickel and tin) were soldered with the cold side of $CoSb_3$ dices to achieve 2 × 2 × 6 mm^3 p-type Bi_2Te_3/$CoSb_3$ segmented joints. Finally, the n-type Ni/Ti/$Mg_3(Sb,Bi)_2$/Ti/Ni joints and p-type Ni/TiAl/$CoSb_3$/Sn/Ni/Bi_2Te_3/Ni/Sn joints were alternately patterned and then connected to DBC alumina plates (10 × 10 × 1 mm^3). Notably, the hot side of the thermoelectric joints was soldered using our newly developed low-temperature assembly technology[29]. Specifically, we utilized a silver nanocomposite paste to achieve connections at low temperatures and low pressure, while yet withstanding higher service temperatures. Prior to measuring the power generation performance, glass fibers were inserted between the thermoelectric legs to minimize heat dissipation. The total internal resistance of the two-pair module is 71 mΩ at room temperature, which includes the resistance from the electrodes and

soldering. The resistance of each thermoelectric joint and contact resistivity of each interface are shown in Supplementary Table 6. The single Mg_3Sb_2-based leg used for reliability assessment was fabricated by a similar process, but its dimensions are $5 \times 5 \times 10$ mm^3. Note that the power cost ratios in Fig. 1e are calculated by the method employed in our previous work[5].

Material and device characterization

The phase composition and crystal structure were characterized by powder X-ray diffraction (XRD, Rigaku D/Max-2550 PC) using Cu-Kα radiation ($\lambda = 1.541$ Å) at 40 kV and 30 mA. The microstructure and chemical composition were analyzed by field emission scanning electron microscopy (FE-SEM, TESCAN/MAIA3, Czech Republic) and transmission electron microscopy (TEM, Hitachi-HF5000) with an energy dispersive spectrometer (EDS). The interfacial contact resistivity was measured using a four-probe measurement system[27]. At least three different positions were measured on each sample to obtain an average value of the contact resistivity. The power generation performance of the thermoelectric single-legs and modules was measured by a commercial measurement system developed by Shanghai Fuyue Vacuum Technology Ltd. This measurement system was calibrated against a commercial Mini-PEM apparatus (Ulvac-Riko, Japan) at the Southern University of Science and Technology before it was put into operation[5]. The efficiency uncertainty is ~10%[5,29,63].

Finite element simulation

The geometrical configuration of the Mg_3Sb_2-based thermoelectric module was optimized using three-dimensional finite element analysis in COMSOL. A full-parameter model coupling the thermoelectric effects (conduction, Joule effect, Thomson effect, and Peltier effect) and comprehensively considering temperature-dependent material properties was used for accurate simulation[5,27].

DFT calculations

All density functional theory calculations were conducted using the *Vienna* Ab initio *Simulation* Package[64]. The calculations employed a plane-wave basis and projector augmented wave method pseudopotentials. To account for exchange-correlation effects, the Perdew-Burke-Ernzerhof generalized gradient approximation was applied[65]. A cut-off of 380 eV was imposed on the kinetic energy. Sampling of the Brillouin zone was carried out using Monkhorst-Pack grids. The accuracy of the total energy was set to 10^{-6} eV. Atomic and lattice parameter relaxations were optimized using a conjugate-gradient algorithm, with a numerical threshold of 0.01 eV/Å. The energy barriers for atom migration (E_{Mig}) to neighboring vacancies were determined using the CI-NEB method with eight inserted images[54]. The interfaces between Mg_3SbBi and Ti-based compounds were constructed by combining the (001) plane of Mg_3SbBi with the low-index plane of the interface compounds, ensuring that the interface mismatch was controlled to be less than 5%.

Data availability

The authors declare that the data supporting the findings of this study are available within the paper and its supplementary information files and the data that support the findings of this study are available from the corresponding author upon reasonable request.

References

1. Yan, Q. & Kanatzidis, M. G. High-performance thermoelectrics and challenges for practical devices. *Nat. Mater.* **21**, 503–513 (2022).
2. Hu, H. et al. Highly stabilized and efficient thermoelectric copper selenide. *Nat. Mater.* **23**, 527–534 (2024).
3. Yu, Y., Xu, X., Bosman, M., Nielsch, K. & He, J. Germanium-telluride-based thermoelectrics. *Nat. Rev. Electr. Eng.* **1**, 109–123 (2024).
4. Gu, M. et al. A high-throughput strategy to screen interfacial diffusion barrier materials for thermoelectric modules. *J. Mater. Res.* **34**, 1179–1187 (2019).
5. Fu, Y. et al. $Mg_3(Bi,Sb)_2$-based thermoelectric modules for efficient and reliable waste-heat utilization up to 750. *K. Energy Environ. Sci.* **15**, 3265–3274 (2022).
6. Xing, T. et al. High efficiency GeTe-based materials and modules for thermoelectric power generation. *Energy Environ. Sci.* **14**, 995–1003 (2021).
7. Liu, M. et al. Screening metal electrodes for thermoelectric PbTe. *ACS Appl. Mater. Interfaces* **15**, 6169–6176 (2023).
8. Chu, J. et al. Electrode interface optimization advances conversion efficiency and stability of thermoelectric devices. *Nat. Commun.* **11**, 2723 (2020).
9. Liu, R. et al. Thermal-inert and ohmic-contact interface for high performance half-Heusler based thermoelectric generator. *Nat. Commun.* **13**, 7738 (2022).
10. Yang, J. et al. Next-generation thermoelectric cooling modules based on high-performance $Mg_3(Bi,Sb)_2$ material. *Joule* **6**, 193–204 (2022).
11. Xie, L. et al. Screening strategy for developing thermoelectric interface materials. *Science* **382**, 921–928 (2023).
12. Yin, L. et al. CALPHAD accelerated design of advanced full-Zintl thermoelectric device. *Nat. Commun.* **15**, 1468 (2024).
13. Gromov, D. G. et al. Mo/Ni and Ni/Ta–W–N/Ni thin-film contact layers for $(Bi,Sb)_2Te_3$-based intermediate-temperature thermoelectric elements. *Inorg. Mater.* **52**, 1132–1136 (2016).
14. Liang, Z. et al. Enhanced thermoelectric performance of p-Type Mg_3Sb_2 for reliable and low-cost all-Mg_3Sb_2-based thermoelectric low-grade heat recovery. *Adv. Funct. Mater.* **33**, 2210016 (2023).
15. Chen, L., Mei, D., Wang, Y. & Li, Y. Ni barrier in Bi_2Te_3-based thermoelectric modules for reduced contact resistance and enhanced power generation properties. *J. Alloy. Compd.* **796**, 314–320 (2019).
16. Mao, J. et al. High thermoelectric cooling performance of n-type Mg_3Bi_2-based materials. *Science* **365**, 495–498 (2019).
17. Zhang, Q. et al. Thermoelectric devices for power generation: recent progress and future challenges. *Adv. Eng. Mater.* **18**, 194–213 (2016).
18. Sun, Y. et al. Performance boost for bismuth telluride thermoelectric generator via barrier layer based on low Young's modulus and particle sliding. *Nat. Commun.* **14**, 8085 (2023).
19. Liu, Y. et al. Mg compensating design in the melting-sintering method for high-performance $Mg_3(Bi,Sb)_2$ thermoelectric devices. *Small* **19**, 2303840 (2023).
20. Ying, P. et al. Towards tellurium-free thermoelectric modules for power generation from low-grade heat. *Nat. Commun.* **12**, 1121 (2021).
21. Bu, Z. et al. An over 10% module efficiency obtained using non-Bi_2Te_3 thermoelectric materials for recovering heat of <600 K. *Energy Environ. Sci.* **14**, 6506–6513 (2021).
22. Ando, F. et al. Dual-boost thermoelectric power generation in a GeTe/Mg_3Sb_2-based module. *Mater. Today Phys.* **36**, 101156 (2023).
23. Wang, Y. et al. Suppression of interfacial diffusion in Mg_3Sb_2 thermoelectric materials through an $Mg_{4.3}Sb_3Ni/Mg_{3.2}Sb_2Y_{0.05}/Mg_{4.3}Sb_3Ni$-graded structure. *ACS Appl. Mater. Interfaces* **14**, 33419–33428 (2022).
24. Liu, Z. et al. Demonstration of ultrahigh thermoelectric efficiency of similar to 7.3% in Mg_3Sb_2/MgAgSb module for low-temperature energy harvesting. *Joule* **5**, 1196–1208 (2021).
25. Liu, Z. et al. Maximizing the performance of n-type Mg_3Bi_2 based materials for room-temperature power generation and thermoelectric cooling. *Nat. Commun.* **13**, 1120 (2022).
26. Li, X. et al. Realizing an excellent conversion efficiency of 14.5% in the Mg_3Sb_2/GeTe-based thermoelectric module for waste heat recovery. *Energy Environ. Sci.* **16**, 6147–6154 (2023).

27. Zhang, Q. et al. Realizing a thermoelectric conversion efficiency of 12% in bismuth telluride/skutterudite segmented modules through full-parameter optimization and energy-loss minimized integration. *Energy Environ. Sci.* **10**, 956–963 (2017).
28. Xie, L. et al. Lead-free and scalable GeTe-based thermoelectric module with an efficiency of 12. *Sci. Adv.* **9**, eadg7919 (2023).
29. Jiang, M. et al. High-efficiency and reliable same-parent thermoelectric modules using Mg_3Sb_2-based compounds. *Natl Sci. Rev.* **10**, nwad095 (2023).
30. Ying, P., Reith, H., Nielsch, K. & He, R. Geometrical optimization and thermal-stability characterization of Te-free thermoelectric modules based on MgAgSb/$Mg_3(Bi,Sb)_2$. *Small* **18**, 2201183 (2022).
31. Bu, Z. et al. A record thermoelectric efficiency in tellurium-free modules for low-grade waste heat recovery. *Nat. Commun.* **13**, 237 (2022).
32. Zhu, Q., Song, S., Zhu, H. & Ren, Z. Realizing high conversion efficiency of Mg_3Sb_2-based thermoelectric materials. *J. Power Sources* **414**, 393–400 (2019).
33. Liang, Z. et al. High thermoelectric energy conversion efficiency of a unicouple of n-type Mg_3Bi_2 and p-type Bi_2Te_3. *Mater. Today Phys.* **19**, 100413 (2021).
34. Chen, S. et al. Thermoelectric and mechanical characterization of the utilization of FeTe as an electrode for iodine-doped PbTe. *J. Alloy. Compd.* **905**, 164267 (2022).
35. Jia, B. et al. Realizing high thermoelectric performance in non-nanostructured n-type PbTe. *Energy Environ. Sci.* **15**, 1920–1929 (2022).
36. Jiang, B. et al. Realizing high-efficiency power generation in low-cost PbS-based thermoelectric materials. *Energy Environ. Sci.* **13**, 579–591 (2020).
37. Jood, P., Ohta, M., Yamamoto, A. & Kanatzidis, M. G. Excessively doped PbTe with Ge-induced nanostructures enables high-efficiency thermoelectric modules. *Joule* **2**, 1339–1355 (2018).
38. Hu, X. et al. Power generation from nanostructured PbTe-based thermoelectrics: comprehensive development from materials to modules. *Energy Environ. Sci.* **9**, 517–529 (2016).
39. Jiang, B. et al. High-entropy-stabilized chalcogenides with high thermoelectric performance. *Science* **371**, 830–834 (2021).
40. Wang, X. et al. Band modulation and strain fluctuation for realizing high average *zT* in GeTe. *Adv. Energy Mater.* **12**, 2201043 (2022).
41. Koenig, J. et al. Thermoelectric efficiency of (1–x)(GeTe) x($Bi_2Se_{0.2}Te_{2.8}$) and implementation into highly performing thermoelectric power generators. *Dalton Trans.* **44**, 2835–2843 (2015).
42. Jiang, B. et al. High figure-of-merit and power generation in high-entropy GeTe-based thermoelectrics. *Science* **377**, 208–213 (2022).
43. Dong, J. et al. High thermoelectric performance in GeTe with compositional insensitivity. *Nano Energy* **103**, 107809 (2022).
44. Jiang, Y. et al. Evolution of defect structures leading to high ZT in GeTe-based thermoelectric materials. *Nat. Commun.* **13**, 6087 (2022).
45. Perumal, S. et al. Realization of high thermoelectric figure of merit in GeTe by complementary co-doping of Bi and In. *Joule* **3**, 2565–2580 (2019).
46. Pei, J. et al. Design and fabrication of segmented GeTe/$(Bi,Sb)_2T_3$ thermoelectric module with enhanced conversion efficiency. *Adv. Funct. Mater.* **33**, 2214771 (2023).
47. Li, M. et al. Roles of anion sites in high-performance GeTe thermoelectrics. *Adv. Funct. Mater.* **32**, 2208579 (2022).
48. Qiu, P. et al. High-efficiency and stable thermoelectric module based on liquid-like materials. *Joule* **3**, 1538–1548 (2019).
49. Wu, X. et al. Interface engineering boosting high power density and conversion efficiency in $Mg_2Sn_{0.75}Ge_{0.25}$-based thermoelectric devices. *Adv. Energy Mater.* **13**, 2301350 (2023).
50. Chen, J. et al. Improvement of stability in a Mg_2Si-based thermoelectric single-leg device via $Mg_{50}Si_{15}Ni_{50}$ barrier. *J. Alloy. Compd.* **926**, 166888 (2022).
51. Geng, Y. et al. Inhibiting Mg diffusion and evaporation by forming Mg-rich reservoir at grain boundaries improves the thermal stability of n-Type Mg_3Sb_2 thermoelectrics. *Small* **20**, 2305670 (2023).
52. Xu, C. et al. Realizing high energy conversion efficiency in a novel segmented-$Mg_3(Sb,Bi)_2$/Cubic-GeTe thermoelectric module for power generation. *Adv. Energy Mater.* **12**, 2202392 (2022).
53. Smigelskas, A. D. & Kirkendall, E. O. Zinc diffusion in alpha brass. *Trans AIME* **171**, 130–142 (1947).
54. Henkelman, G., Uberuaga, B. P. & Jónsson, H. A climbing image nudged elastic band method for finding saddle points and minimum energy paths. *J. Chem. Phys.* **113**, 9901–9904 (2000).
55. Wu, X. et al. Interface and surface engineering realized high efficiency of 13% and improved thermal stability in $Mg_3Sb_{1.5}Bi_{0.5}$-based thermoelectric generation devices. *Adv. Energy Mater.* **12**, 2203039 (2022).
56. Zhang, J., Jorgensen, L. R., Song, L. & Iversen, B. B. Insight into the strategies for improving the thermal stability of efficient n-Type Mg_3Sb_2-based thermoelectric materials. *ACS Appl. Mater. Interfaces* **14**, 31024–31034 (2022).
57. Gu, M. et al. Study on the high temperature interfacial stability of Ti/Mo/$Yb_{0.3}Co_4Sb_{12}$ thermoelectric joints. *Appl. Sci.* **7**, 952 (2017).
58. Stradi, D. et al. General atomistic approach for modeling metal-semiconductor interfaces using density functional theory and nonequilibrium Green's function. *Phys. Rev. B* **93**, 155302 (2016).
59. Zhang, Z. et al. Plastic $Mg_3(Sb,Bi)_2$-based thermoelectric compounds with enhanced texture via cold-deformation. *J. Mater. Chem. A* **12**, 8893–8899 (2024).
60. Li, A. et al. High performance magnesium-based plastic semiconductors for flexible thermoelectrics. *Nat. Commun.* **15**, 5108 (2024).
61. Zhao, P. et al. Plasticity in single-crystalline Mg_3Bi_2 thermoelectric material. *Nature* **631**, 777–782 (2024).
62. Zhang, Q. et al. Realizing high-performance thermoelectric power generation through grain boundary engineering of skutterudite-based nanocomposites. *Nano Energy* **41**, 501–510 (2017).
63. Lu, X. et al. High-efficiency thermoelectric power generation enabled by homogeneous incorporation of MXene in $(Bi, Sb)_2Te_3$ matrix. *Adv. Energy Mater.* **10**, 1902986 (2020).
64. Kresse, G. & Furthmüller, J. Efficient iterative schemes for ab initio total-energy calculations using a plane-wave basis set. *Phys. Rev. B* **54**, 11169–11186 (1996).
65. Perdew, J. P., Burke, K. & Ernzerhof, M. Generalized gradient approximation made simple. *Phys. Rev. Lett.* **77**, 3865–3868 (1996).
66. Wu, X. et al. A general design strategy for thermoelectric interface materials in n-type $Mg_3Sb_{1.5}Bi_{0.5}$ single leg used in TEGs. *Acta Mater.* **226**, 117616 (2022).
67. Yin, L. et al. Reliable n-type $Mg_{3.2}Sb_{1.5}Bi_{0.49}Te_{0.01}$/304 stainless steel junction for thermoelectric applications. *Acta Mater.* **198**, 25–34 (2020).
68. Qu, N. et al. Interfacial design contributing to high conversion efficiency in $Mg_3(Sb,Bi)_2/Bi_2Te_3$ thermoelectric module with superior stability. *Adv. Energy Mater.* **14**, 2302818 (2023).
69. Li, J. et al. Bi-deficiency leading to high-performance in $Mg_3(Sb,Bi)_2$-based thermoelectric materials. *Adv. Mater.* **35**, 2209119 (2023).
70. Chen, N. et al. Improved figure of merit (z) at low temperatures for superior thermoelectric cooling in $Mg_3(Bi,Sb)_2$. *Nat. Commun.* **14**, 4932 (2023).

Acknowledgements

This work was financially supported by the National Natural Science Foundation of China (No. U23A20685, 52174343, 52272256), the Innovation Program of Shanghai Municipal Education Commission

(202101070003E00110), and Shanghai Committee of Science and Technology (23520710300 and 22ZR1471400). X.L. acknowledges the financial support from Shanghai 2023 "Science and Technology Innovation Action Plan" Sailing Program (23YF1400200).

Author contributions

Y.F., Q.Z., and L.W. conceived the ideas and designed the work. Y.F. and Z.H. carried out the experiments including material preparation and characterization, device fabrication, and measurements. X.A. contributed to material preparation and interface design. Y.F., X.A., and A.H. performed the device simulations. J.H. conducted the DFT calculations. Y.F., Q.Z., X.A., and J.H. wrote the draft. S.Z., X.L., L.W., and W.J. contributed to the discussion and editing. All authors reviewed and commented on the manuscript.

Competing interests

The authors declare no competing interests.

Additional information

Supplementary information The online version contains supplementary material available at https://doi.org/10.1038/s41467-024-53598-3.

Correspondence and requests for materials should be addressed to Jian Huang, Lianjun Wang, Qihao Zhang or Wan Jiang.

Peer review information *Nature Communications* thanks Chia-Jyi Liu, Yuan Yu and the other anonymous reviewer(s) for their contribution to the peer review of this work. A peer review file is available.

Reprints and permissions information is available at http://www.nature.com/reprints

Publisher's note Springer Nature remains neutral with regard to jurisdictional claims in published maps and institutional affiliations.

Open Access This article is licensed under a Creative Commons Attribution-NonCommercial-NoDerivatives 4.0 International License, which permits any non-commercial use, sharing, distribution and reproduction in any medium or format, as long as you give appropriate credit to the original author(s) and the source, provide a link to the Creative Commons licence, and indicate if you modified the licensed material. You do not have permission under this licence to share adapted material derived from this article or parts of it. The images or other third party material in this article are included in the article's Creative Commons licence, unless indicated otherwise in a credit line to the material. If material is not included in the article's Creative Commons licence and your intended use is not permitted by statutory regulation or exceeds the permitted use, you will need to obtain permission directly from the copyright holder. To view a copy of this licence, visit http://creativecommons.org/licenses/by-nc-nd/4.0/.

© The Author(s) 2024